Transport and Entrapment of Particles in Continuous Casting of Steel

Quan Yuan
American Air Liqiude, Chicago Research Center
5230 S. East Ave., Countryside, IL, 60525
Tel: 708-579-7812, Fax: 708-579-7833
quan.yuan@airliquide.com

Brian G. Thomas
University of Illinois at Urbana-Champaign
Department of Mechanical and Industrial Engineering
1206 W. Green St., Urbana, IL, 61801, U.S.A.
Tel: 217-333-6919, Fax: 217-244-6534
bgthomas@uiuc.edu

ABSTRACT

The entrapment of inclusions, bubbles, slag, and other particles into solidified steel products is a critically-important quality concern. During continuous casting, particles may enter the mold with the steel flowing through the submerged nozzle. In addition, mold slag may be entrained from the top surface. A computational model has been developed to simulate the transport and entrapment of particles from both of these sources. The model first computes transient turbulent flow in the mold region using Large Eddy Simulation (LES), with the sub-grid-scale (SGS) k model. Next, the transport and capture of over 30,000 particles are simulated using a Lagrangian approach to track the trajectories. A new criterion was developed to model particle pushing and capture by a dendritic interface and was incorporated into the particle transport model. Particles smaller than the primary dendrite arm spacing are entrapped if they enter the boundary layer region and touch the solidifying steel shell. Larger particles are entrapped only if they remain stable while the shell grows around them. The new criterion models this by considering a balance of ten different forces which act on a particle in the boundary layer region, including the bulk hydrodynamic forces (lift, pressure gradient, stress gradient, Basset, and added mass forces), transverse drag force, (caused by fluid flow across the dendrite interface), gravity (buoyancy) force, and the forces acting at the interface (Van der Waals interfacial force, lubrication drag force, and surface energy gradient force). The criterion was validated by reproducing experimental results in two different systems. Finally, the model was used to predict the entrapment distributions, removal rates, and fractions of different sized particles in a straight-walled thin slab caster. Although more large particles are safely removed than small ones, the capture rate as defects is still very high.

INTRODUCTION

The entrapment of inclusions, bubbles, slag, and other particles during solidification of steel products is a critically-important quality concern. These particles require the finished product to undergo expensive inspection, surface grinding and even rejection. Furthermore, if undetected, large particles lower the fatigue life, while captured bubbles and inclusion clusters cause slivers, blisters, and other surface defects in rolled products. During continuous casting, particles may enter the mold with the steel flowing through the submerged nozzle. In addition, mold slag may be entrained from the top surface. The fraction of these particles which ultimately end up entrapped in the solidified shell has not previously been quantified.

A computational model has been developed to simulate the transport and entrapment of particles from both of these sources. The model first computes transient turbulent flow in the mold region using Large Eddy Simulation (LES), with a sub-grid-scale (SGS) k model. Next, the transport and capture of over 30,000 particles are simulated using a Lagrangian approach to track the trajectories. The entrapment of particles which touch the boundaries representing the solidifying shell is determined by evaluating a force balance on each particle that resides in the fluid boundary layer at the dendritic interface.

A schematic of the steel continuous casting process is depicted in **Fig. 1** [1], with a close-up of the simulated regions of the nozzle and liquid-pool of the continuous casting mold and upper strand given in **Fig. 2**. Steel flows from the ladle, through the tundish and into the mold through a submerged netry nozzle. Jets of molten steel exit the nozzle ports and traverse across the mold cavity to impinge on the solidifying steel shell near the narrow faces. These jets carry bubbles and inclusion particles into the mold cavity. In addition, high speed flow across the top surface may shear droplets of liquid mold slag into the flow, where they may become entrained in the liquid steel [2]. If the flow pattern enables the particles to reach the top surface, they should be harmlessly removed into the liquid slag layer, so long as the slag is not saturated and the surface tension forces are not excessive. However, when the flow pattern is detrimental, particles become entrapped in the solidifying steel shell, where they cause serious quality problems and costly rejects. Particle trajectories and removal depend on particle size, which is further complicated by collisions and attachment to bubbles. Particles that become trapped near the meniscus generate surface delamination defects, and may initiate surface cracks. This problem is more likely when there are rapid fluctuations in the level of the top surface. It is also more likely when the meniscus partially freezes to form meniscus "hooks", which entrap particles into the solidifying meniscus before they can enter the liquid slag. Meniscus hooks are more prevalent there is insufficient liquid temperature at the meniscus. The local superheat of the molten steel near the meniscus depends on the flow pattern in the mold, as the jets also transport superheat.
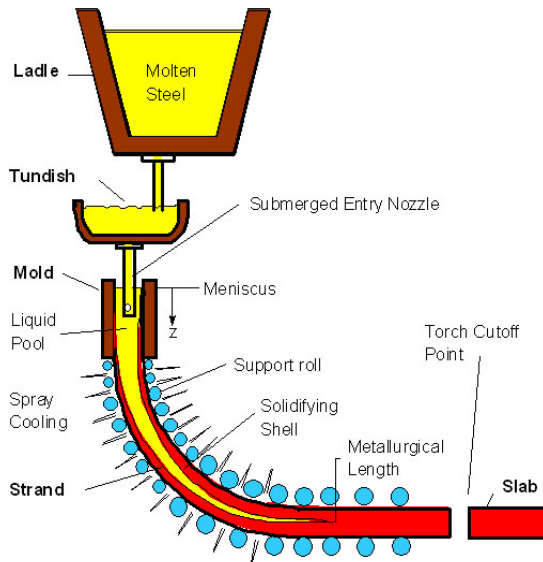

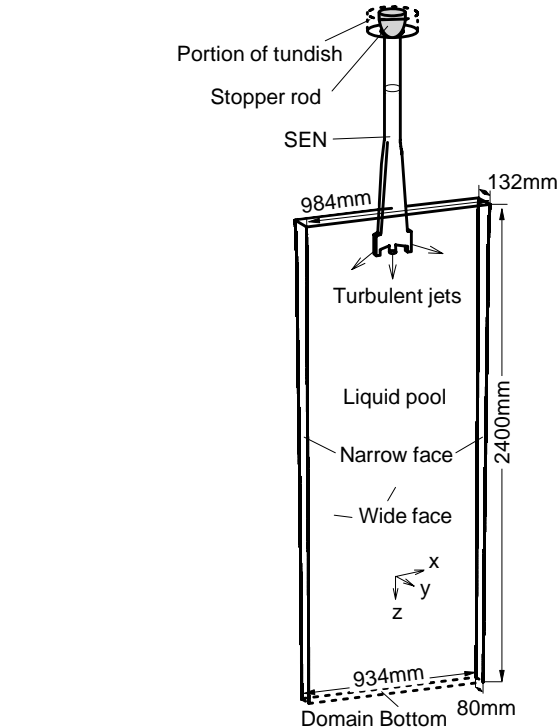**Fig. 1**. Schematic of Steel Processing including ladle, tundish, and continuous casting

Fig. 2. Schematic of the computational domain of the thin-slab steel caster, including tundish nozzle.

High velocities across the meniscus are detrimental because they cause excessive surface level fluctuations, which enhances particle entrapment. High surface velocities also may entrain some of the molten slag into the steel, where it breaks up into slag inclusions. This is also controlled by the flow pattern in the mold.

Particles which are entrained into the lower recirculation zones can gradually spiral and become trapped in the solidifying front deep inside the product,[3, 4] leading to internal cracks, slivers in the final rolled product, and blisters.[5] One of these defects, known as "pencil pipes"[2] is caused when small argon gas bubbles surrounded by inclusions are caught in the solidifying shell. During rolling, the inclusion clusters elongate to create long slivers in the final product. During subsequent annealing processes, the trapped bubbles expand to create surface blisters [2]. These intermittent defects are particularly costly because they are often not detected until after many subsequent finishing steps.

There is clearly a great incentive to understand how to control the mold flow pattern in order to minimize particle entrapment and the associated quality problems. Should flow-pattern design focus on directing inclusions to the top surface to enhance their removal, or should it focus on avoiding other problems, such as entrainment of slag at the surface, level fluctuations, and meniscus defects? To answer this and related questions requires consideration of many different phenomena that may contribute to the defects, whose relative importance and mechanisms need to be quantified. This is the subject of the current work.

FLUID FLOW MODEL DESCRIPTION AND VALIDATION

A Large Eddy Simulation (LES) computer model has been developed to accurately simulate the details of transient turbulent flow and particle motion in the molten steel pool of the continuous casting nozzle and strand in three-dimensions [6]. The time-dependent three-dimensional Navier-Stokes equations are discretized using the Harlow-Welch fractional step procedure [7]. Second order central differencing is used for the convection terms and the Crank-Nicolson scheme [8] is used for the diffusion terms. The Adams-Bashforth scheme [9] is used to discretize in time with second order accuracy. The pressure Poisson equation is solved using an algebraic multi-grid (AMG) solver [10]. A sub-grid turbulent kinetic energy model [11] is employed to represent the effects of the unsolved small eddies. A complete description of this model can be found elsewhere [12, 13].

The mesh and domain used for this study was chosen from a rigorous investigation of mesh and time step refinement [13, 14]. To quantify the difference between grids on an equal basis, the velocities computed for each grid were first interpolated onto a 64x128 uniform-spaced grid. Errors for both the time-average and rms velocity were calculated as an average at the center plane y = 0 where the exact solution was estimated using the results from the finest grid (0.8 million cells).

The time average error results are presented in **Fig. 3a.** This error increases drastically with increasing grid spacing, which corresponds with decreasing number of cells in the grid. The error between the two finest grids averages only ~0.03m/s, although this represents a 17% difference, relative to the mean velocity in the domain, ~0.18m/s. Coarser grids have errors that are much larger than a glance at the velocity vectors would indicate.

The rms velocity error results are presented in **Fig. 3b**. This error also increases greatly with coarsening grid size. These results indicate that the mesh resolution prediction of velocity fluctuations is accurate within ~0.02m/s or ~17%. The fluctuating velocity component is almost half of the mean velocity component, indicating that turbulence is very strong. Overall, the fine mesh (0.8 million nodes) is believed to produce reasonable results for engineering purposes. A mesh of this refinement was used in subsequent simulations. Further details can be found elsewhere [13, 14].
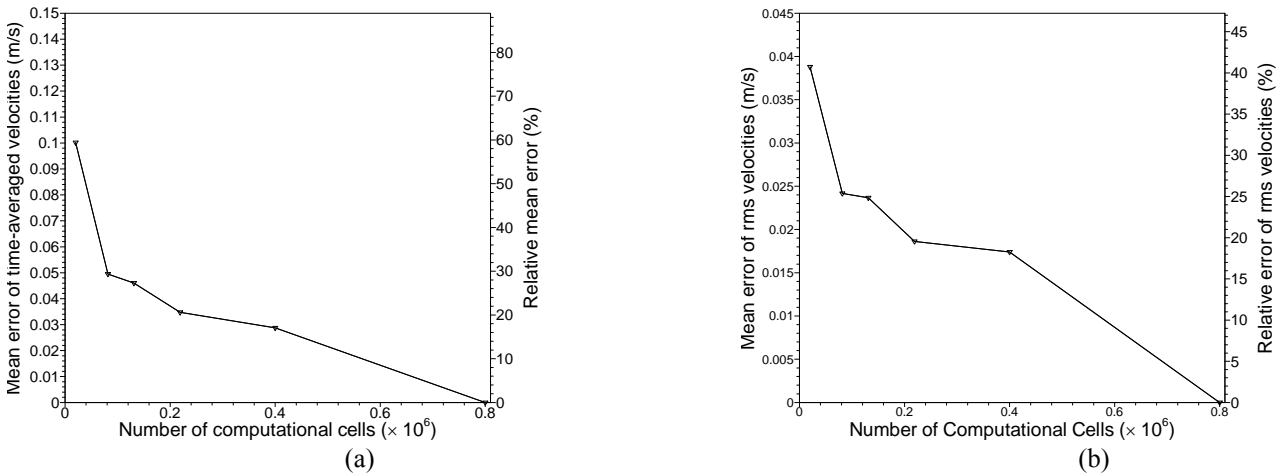

(a)   (b)

Fig. 3.   Effect of grid refinement on error in (a) time-averaged and (b) *rms* velocities.

PARTICLE TRANPORT MODEL DESCRIPTION AND VALIDATION

The Large-Eddy Simulation program for computing fluid flow was extended to simulate the transient transport and entrapment of inclusion particles, based on previous computations of fluid flow in the continuous steel casting process [15]. A Lagrangian approach was developed to simulate the transport of large groups of particles through the transient flow fields. Past work on this project demonstrated validation of models of both the fluid flow and the transport of small particles using measurements in both water models and analysis of actual steel samples. The results of transport and capture of small inclusions (10μm and 40μm) in a thin-slab steel caster are described in detail elsewhere [16]. This work showed that most of the small particles entering the mold are captured in the final product. The present work investigates the more difficult issue of the transport and entrapment of large particles, which are a greater concern for product quality.

The geometry and operating conditions of the thin-slab caster are given in Fig. 2 and Table I. Fluid flow and particle transport were computed in the model domain (that includes the 1.11m submerged entry nozzle and the top 2.40m of a steel strand. Three dimensional time-dependent turbulent fluid velocities were first obtained by solving the Navier-Stokes equations using large eddy simulations (LES) [15]. Special velocity boundary conditions [15] were applied to the fluid at the solidifying front in the steel caster to simulate the solidification effects. The transport of inclusion particles through this flow field was then modeled as follows.

Governing Equations for Particle Motion

The motions of spherical inclusion particles during continuous steel casting can be simulated by integrating the following transport equation for each particle:

$$\frac{d\mathbf{x}_p}{dt} = \mathbf{v}_p \tag{1}$$

$$m_p \frac{d\mathbf{v}_p}{dt} = \mathbf{F}_D + \mathbf{F}_L + \mathbf{F}_{Press} + \mathbf{F}_{stress} + \mathbf{F}_A + \mathbf{F}_H + \mathbf{F}_G \tag{2}$$

where the terms on the right hand side (RHS) in Eq. (2) are the steady-state drag force, the lift force, the pressure gradient force, the stress gradient force, the added mass force, the Basset history force and the gravitational force. Because the sizes of the particles interested in this work are small ($\leq\sim10^2\mu$m), extra terms arising from the non-uniformity of the flow can be neglected. Further details on each of the six hydrodynamic forces in Eq. (2) are given next.

1) <u>Drag Force</u>. The drag force acting on a small sphere in a uniform flow can be expressed as: [17]

$$\mathbf{F}_D = \frac{1}{8}\pi d_p^2 \rho_f C_D \left|\mathbf{v}_f - \mathbf{v}_p\right|\left(\mathbf{v}_f - \mathbf{v}_p\right) \tag{3}$$

where:
$$C_D = f_{Re_p}\left(24\Big/Re_p\right) \quad \text{and} \tag{4}$$

$$Re_p = \left|\mathbf{v}_f - \mathbf{v}_p\right|d_p\Big/\nu \tag{5}$$

in which v_f and v_p are the fluid and particle velocities, C_D is the drag coefficient and f_{Rep} is the correction factor due to a finite particle Reynolds number, which can be found through Eq. (6) for $Re_p\leq800$: [17]

$$f_{Re_p} = \left(1 + 0.15\,Re_p^{0.687}\right) \tag{6}$$

2) <u>Shear Lift Force</u>. Saffman [18] derived the lift force on solid spheres in an unbounded linear shear flow with the following form:

$$F_{L,Saff} = 1.61\mu d_p \left|\mathbf{v}_f - \mathbf{v}_p\right|\sqrt{Re_G} \tag{7}$$

$$Re_G = Gd_p^2\Big/\nu \tag{8}$$

where G is the velocity gradient. It was assumed in Saffman's derivation that both the particle Reynolds number Re_p and the shear Reynolds number Re_G are much less than unity and $Re_p \ll \sqrt{Re_G}$. Equation (7) can also be written as follows:

$$\mathbf{F}_{L,Saff} = 1.61d_p^2\left(\mu\rho\right)^{1/2}\left|\nabla\times\mathbf{v}_f\right|^{-1/2}\left[\left(\mathbf{v}_f - \mathbf{v}_p\right)\times\left(\nabla\times\mathbf{v}_f\right)\right] \tag{9}$$

Corrections due to a finite Reynolds number and the near-wall effects were derived by McLaughlin: [19, 20]

$$F_L\Big/F_{L,Saff} = 0.443J(\varepsilon,l^*) \tag{10}$$

where:
$$\varepsilon = \sqrt{Re_G}\big/Re_p \tag{11}$$

$$l^* = l_w\left(G\Big/\nu\right)^{1/2} \tag{12}$$

Because of the complexity of the general expression for J, [21] Mei [22] reconstructed it for particles far from the wall [21] using curve fitting for $0.1\leq\varepsilon\leq20$:

$$J(\varepsilon) \approx 0.6765\left\{1 + \tanh\left[2.5\log_{10}\varepsilon + 0.191\right]\right\}\left\{0.667 + \tanh\left[6\left(\varepsilon - 0.32\right)\right]\right\} \tag{13}$$

If the particle is close to the wall ($l^*\leq0.1$), $J(\varepsilon, l^*)$ can be computed by: [20]

$$J(\varepsilon) = \frac{\pi^2}{16}\left(\frac{1}{\varepsilon} + \frac{11}{6}l^*\right)$$

(14)

Derivations and discussions on the lift force corrections can be found in [20, 22, 23].

3) Pressure Gradient and Stress Gradient Forces. The pressure gradient force, which contributes to the hydrostatic component of the buoyancy, can be important when the particle density is comparable or lighter than the fluid. It can be calculated through the following equation: [17]

$$\mathbf{F}_{press} = -\frac{\pi d_p^3}{6}\nabla p$$

(15)

By applying the divergence theorem, a similar expression for the stress gradient force is reached: [17]

$$\mathbf{F}_{stress} = -\frac{\pi d_p^3}{6}\nabla \tau_{ij}$$

(16)

Adding the two forces yields a simple expression as follows:

$$\mathbf{F}_{press} + \mathbf{F}_{stress} = -\frac{\pi d_p^3}{6}\frac{D\mathbf{v}_f}{Dt}$$

(17)

4) Added Mass Force.   Both the added mass force and the Basset history force are unsteady forces due to the acceleration of the particle relative to the surrounding fluid velocity. Previous studies suggest that they might be important for neutral-buoyant particles [24]. These two forces have been neglected in previous studies of particle transport during continuous steel casting. To investigate their importance, they were included in one simulation.

The added mass force arises from the acceleration of the surrounding fluid by the particle.   It can be expressed as follows: [17, 25]

$$\mathbf{F}_A = \frac{C_A \rho \pi d_p^3}{12}\left(\frac{D\mathbf{v}_f}{Dt} - \frac{d\mathbf{v}_p}{dt}\right)$$

(18)

$$C_A = 2.1 - \frac{0.132}{0.12 + Ac^2}$$

(19)

$$Ac = \frac{\left|\mathbf{v}_f - \mathbf{v}_p\right|^2}{d_p \dfrac{d\left|\mathbf{v}_f - \mathbf{v}_p\right|}{dt}}$$

(20)

where C_A is the correction factor due to the acceleration effect and Ac is the acceleration parameter [25].   Note that in Eq. (18), the total derivative, D/Dt is defined as $\frac{\partial}{\partial t} + (\mathbf{v}\cdot\nabla)$.

5) Basset History Force.   The Basset history force is due to the lag of the development of the particle wake [17]. It is formulated as follows: [17, 25]

$$\mathbf{F}_H = \frac{3}{2}C_H d_p^2\sqrt{\pi\rho\mu}\left[\int_0^{t_p}\frac{1}{\sqrt{t_p - t'}}\left(\frac{D\mathbf{v}_f}{Dt'} - \frac{d\mathbf{v}_p}{dt'}\right)dt' + \frac{(\mathbf{v}_f - \mathbf{v}_p)_{t=0}}{\sqrt{t_p}}\right]$$

(21)

$$C_H = 0.48 + \frac{0.52}{(1 + Ac)^2}$$

(22)

where C_H is the correction factor due to the acceleration of the relative velocity [26]. Because all of the particles in this work are introduced into the computational domain with the same velocity as the local fluid, the second term in Eq. (21) always has a value of zero. The Basset integral is evaluated numerically [27].

6) Gravitational Force. Particle buoyancy is incorporated via the upward hydrostatic component of the pressure gradient force and the downward gravity force:

$$\mathbf{F}_g = \frac{1}{6}\pi d_p^3 \rho_p \mathbf{g}$$

(23)

Substituting Eqs. (3), (7), (9), (10), (17), (18), (21) and (23) into Eq. (2) yields the transport equation for particles in a uniform velocity field shown as the follows:

$$\left(1+\frac{C_A\rho}{2\rho_p}\right)\frac{d\mathbf{v}_p}{dt}=\frac{\left(1+0.15\,\mathrm{Re}_p^{0.687}\right)}{\tau_V}\left(\mathbf{v}_f-\mathbf{v}_p\right)+0.07568J\frac{d_p}{\tau_V}\left|\nabla\times\mathbf{v}_f\right|^{-1/2}\left[\left(\mathbf{v}_f-\mathbf{v}_p\right)\times\left(\nabla\times\mathbf{v}_f\right)\right]$$

$$+\left(1+\frac{C_A}{2}\right)\frac{\rho}{\rho_p}\frac{D\mathbf{v}_f}{Dt}+C_H\sqrt{\frac{9}{2\pi}\frac{\rho}{\rho_p}}\frac{1}{\sqrt{\tau_V}}\left[\int_0^{t_p}\frac{1}{\sqrt{t_p-t_p'}}\left(\frac{D\mathbf{v}_f}{Dt_p'}-\frac{d\mathbf{v}_p}{dt_p'}\right)dt_p'+\frac{\left(\mathbf{v}_f-\mathbf{v}_p\right)_{t=0}}{\sqrt{t_p}}\right]+\mathbf{g}\left(1-\frac{\rho}{\rho_p}\right)\quad(24)$$

where τ_V is the particle velocity response time defined as:

$$\tau_V=\frac{\rho_p d_p^2}{18\mu}\qquad(25)$$

Initial simulations were performed to compare the relative importance of these six forces in the bulk flow region [12]. The results reveal that the drag force ($\mathbf{F}_D$) and the buoyancy force ($\mathbf{F}_B$) are always the most significant forces. These two forces, which act in opposite directions, usually almost balance. The pressure gradient and stress gradient force, the added mass force and the Basset history force have approximately the same magnitude, which is usually less than 15 percent of the buoyancy force. This suggests that these three forces could be neglected for engineering calculations. The lift force never exceeded 2-3 percent of the buoyancy so is the least important force in the bulk region.

Initial and Boundary Conditions

Inclusions were introduced into the computational domain at the local fluid velocity. Their initial positions were chosen randomly in the edges of a cylindrical region in the tundish above the submerged entry nozzle. The results of the separate simulation of fluid flow and particle trajectories in the nozzle itself were used to determine the particle locations in the nozzle outlet port planes for the strand simulation. During Lagrangian simulation of the particle trajectories, inclusions touching the top surface were assumed to be removed. Inclusions touching the solidification front were tested for entrapment according to a criterion based on balancing the forces acting upon them.

Boundary Layer Forces on a Particle Close to a Solidication Front

In addition to the six hydrodynamic forces just discussed, five additional forces may act on particles only when they reside in the boundary-layer region and are nearly touching a solidifying dendritic interface. **Fig. 4** illustrates solidifying columnar dendrites, (taken from a phase field model[33]) with a spherical particle positioned in front of the interface. It also shows the five additional forces, which include the lubrication force ($\mathbf{F}_{Lub}$), the Van der Waals interfacial force ($\mathbf{F}_I$), the surface energy gradient forces ($\mathbf{F}_{Grad}$), the reaction force ($\mathbf{F}_N$) and the friction force($\mathbf{F}_f$). It should be noted that the reaction and the friction forces (denoted as dashed lines) do not directly affect particle capture, and the friction force may not even exist. The remaining three forces are only significant when the particle is very close to the solid-liquid boundaries, so were not included in the particle transport Eq. (2).
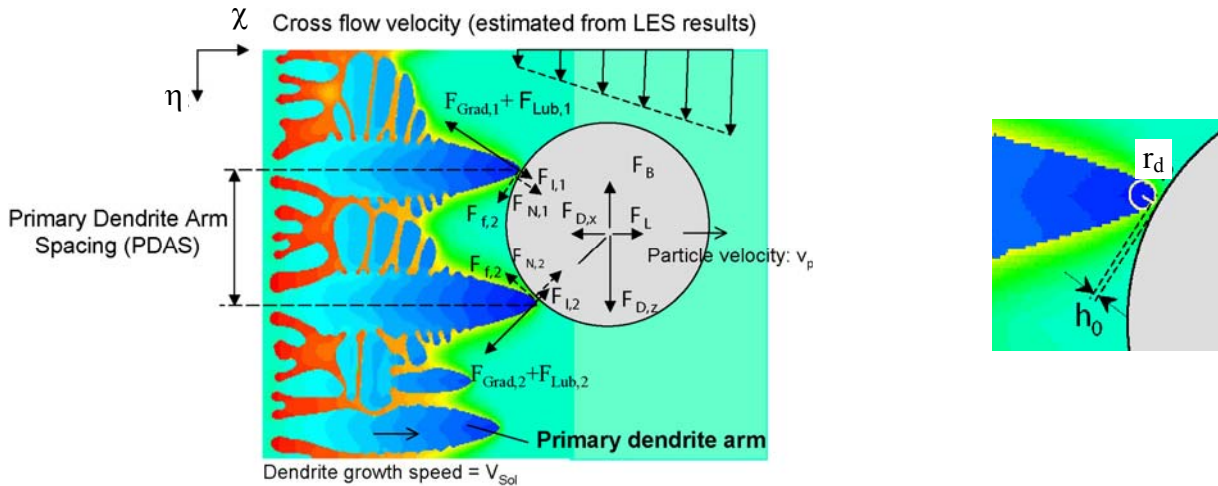

Fig. 4. Illustration of forces acting on a particle in front of a solidifying dendritic interface.

1) Lubrication Force. The lubrication force, $F_{lub,n}$, arises from the simple pressure-driven fluid flow needed to fill the thin gap between the particle and the dendrite tip [28, 29]. This flow is induced at a critical state when the particle moves at the same speed as the solidification front velocity, thus maintaining the steady-state balanced configuration given in Fig. 4. This force acts along the particle radius towards the dendrite tip and must be overcome for the particle to avoid entrapment. The magnitude of this force naturally increases with increasing particle (front) velocity, V_{sol}, decreasing gap thickness, h_0., and increasing dendrite tip radius, r_d, which is typically much smaller than the particle radius, R_p

$$F_{Lub,n} = 6\pi\mu V_{sol} \frac{R_p^2}{h_0}\left(\frac{r_d}{r_d + R_p}\right)^2 \tag{26}$$

2) Van der Waals Force. This weakest of all atomic attraction forces becomes significant when the thin gap between the particle and dendrite tip, h_0, becomes small enough. For a spherical particle "touching" a convex-curved dendrite tip, the Van der Waals interfacial force, F_I, is [30]

$$F_I \square 2\pi\Delta\sigma_0 \frac{r_d R_p}{r_d + R_p} \frac{a_0^2}{h_0^2} \tag{27}$$

$$\Delta\sigma_0 = \sigma_{sp} - \sigma_{sl} - \sigma_{pl} \tag{28}$$

where σ is surface energy, the subscripts s, p and l denote solid, particle and liquid respectively and a_0 is the diameter of a liquid atom. This attraction force encourages particle entrapment.

3) Surface Energy Gradient Force. The surface energy of molten steel depends on temperature and composition. The rejection of solute at the solidifying dendrite tip causes composition gradients in the liquid, which induce surface energy gradients, which create a force on the relatively larger particle. This force is significant and much greater than that from temperature gradients [12]. Alloying elements which are interfacially active, such as sulfur and oxygen, are responsible for this effect. It is shown elsewhere [12] that sulfur is the major solute contributing to this effect in killed steel, where the oxygen content is very low, so the effects of other alloys can be neglected. The surface energy gradient force, F_{grad}, acting on a spherical particle close to a hemispherical dendrite tip is derived to be:

$$F_{Grad} = -\frac{m\beta\pi R_p}{\xi^2}\left\{\frac{(\xi^2 - R_p^2)}{\beta}\ln\left[\frac{(\xi + R_p)[\alpha(\xi - R_p) + \beta]}{(\xi - R_p)[\alpha(\xi + R_p) + \beta]}\right] + \frac{2R_p}{\alpha} - \frac{\beta}{\alpha^2}\ln\left[\frac{\alpha(\xi + R_p) + \beta}{\alpha(\xi - R_p) + \beta}\right]\right\} \tag{29}$$

$$A = 1 + n\,C_S \tag{30}$$

$$\beta = n\,r_d\,(C^* - C_S) \tag{31}$$

$$\xi = R_p + r_d + h_0 \tag{32}$$

The steel surface energy variation with dissolved sulfur concentration is fit to measured data as follows [31] :

$$\sigma_{lv} = \sigma_0 - m\,ln(1 + nC_S) \quad \text{if } C_S \le 0.5 \tag{33}$$

where σ_0, m and n are empirical constants with values of 1.97 J/m^2, 0.17 J/m^2 and 844(wt%)$^{-1}$, C_S (wt%) is the average sulfur content of the steel, and L is the distance between the particle and dendrite tip centers. The elevated sulfur content at the dendrite tip interface, C^*, can be estimated from:

$$V_{sol}\,r_d\,(1-k)\,C^* = 2D(C^* - C_S) \tag{34}$$

Where k is the partition coefficient (0.05) and D is the diffusion coefficient (3.4×10^{-9} m^2/s) of sulfur (at 0.1wt%) in iron. The surface tension acting on the outside of the particle is larger than that at the dendrite tip, where the increased sulfur content lowers the local surface tension. Thus, this force acts along the particle radius towards the dendrite tip center, and encourages particle capture.

Modeling of Particle Capture by the Solidification Front

Particles whose trajectories through the turbulent flowing liquid carry them into the mushy zone front may either be trapped by the solidifying shell or else repulsed back into the molten steel flow. The outcome between capture and pushing depends on many phenomena, including the morphology of the solidifying dendrites, the interfacial surface tension governed by the concentration boundary layer of the interfacial active solutes (especially the sulfur content), the boundary layer velocity profile, and the particle velocity, size, density and morphology. The flow velocities close to the dendritic interface can be estimated from the LES model during the simulation. However, accurate resolution of the dendrite shape and the concentration boundary layer is computationally prohibitive. To overcome this problem, a novel, but simple criterion for particle pushing and capture has been developed in this work, based on a force balance analysis.

Particles Smaller than the PDAS: Particles smaller than the primary dendrite arm spacing (PDAS), (i.e. $2R_p <$ PDAS), can easily flow in between the dendrite arms without major disturbance of their growth. Larger particles cannot do this. If the particle is smaller than the PDAS, it will be surrounded by the growing dendrites, and it will be captured whenever it reaches the solidification front. The attractive force generated by the lubrication, Van der Waals, and surface energy gradient forces further encourages this to happen. Previous experimental studies [32] in quiescent solidification systems confirm that particles smaller than the PDAS are entrapped, even when the dendrite growth speed is much lower than the critical value for particle pushing. Therefore, a particle smaller than the PDAS is modeled as being captured by the shell whenever it touches a computational boundary representing a mushy zone (solidification) interface.

Particles Larger than the PDAS: Unlike smaller particles, particles larger than the local PDAS cannot fit between the dendrite arms. Figure 4 shows a typical dendritic front shape [33]. As depicted in Fig. 4, a spherical particle of alumina or slag transported to the solidification front contacts the solidifying dendrites through a thin film of liquid steel at the critical distance. If all of the forces acting on the particle are in stable equilibrium, then it will eventually be captured by the solidifying shell as the dendrites grow to surround it. The particle will avoid being captured if the net force acting in the solidification direction push it away from the interface, or if the net force acting across the dendrite front causes it to rotate away. These conditions are checked by considering the balance of the ten different forces which act on the particle in the boundary layer region, including transverse drag force F_D, (caused by fluid flow across the dendrite interface), gravity (buoyancy) force F_B, the minor bulk hydrodynamic forces (lift F_L, pressure gradient, stress gradient, Basset, and added mass forces), and the forces acting at the interface (lubrication drag force F_{Lub}, Van der Waals interfacial force F_I, and surface energy gradient force F_{Grad}).

The pressure gradient, stress gradient, Basset, and added mass forces are negligible because they are found to be small (<15% of the buoyancy force) in the bulk region, and are expected to be even smaller in the boundary layer. The condition of particle pushing or capture is determined through the following procedure:

Step 1: If the component of the total force (F_{Tot}) acting on the particle in the solidification direction (χ in Fig. 4) is larger than zero, then the particle will be pushed away from the interface. This escape criterion is expressed as follows:

$$F_{Tot,\chi} = F_L - F_{D,\chi} - 2(F_{Lub} - F_{Grad} - F_I)\cos\theta > 0 \qquad (35)$$

$$\text{where:} \quad \theta = acr\sin\left[0.5\text{PDAS}\Big/\left(R_p + r_d\right)\right] \qquad (36)$$

Otherwise, check if the forces on the particle are large enough to avoid entrapment by pushing it along the interface.

Step 2: If $F_{Tot,\chi} \leq 0$, then the forces acting in η direction (across the solidification front) push the particle against a dendrite arm, causing a reaction force ($F_{N,1}$ or $F_{N,2}$) and a friction force ($F_{f,1}$ or $F_{f,2}$) at the contact point, as shown in Fig. 4. If furthermore, the net forces rotating the particle about the contact points push it towards the dendrites, then the particle will not move and it will eventually become surrounded by the growing interface and captured. Specifically, capture occurs by this criterion if one of the following two conditions holds:

(1) If the buoyancy (F_B) and the η component of the drag ($F_{D,\eta}$) are in the same direction and:

$$(F_{D,\eta} + F_{B,\eta})\cos\theta + (F_L - F_\chi)\sin\theta \leq (F_{Lub} - F_{Grad} - F_I)\sin 2\theta \qquad (37)$$

(2) If the buoyancy (F_B) and the η component of the drag ($F_{D,\eta}$) are in opposite directions, and either:

$$(F_{D,\eta} - F_B)\cos\theta + (F_L - F_\chi)\sin\theta \leq (F_{Lub} - F_{Grad} - F_I)\sin 2\theta, \text{ if } F_{D,\eta} \geq F_B \qquad (38)$$

$$\text{or} \quad (F_B - F_{D,\eta})\cos\theta + (F_L - F_\chi)\sin\theta \leq (F_{Lub} - F_{Grad} - F_I)\sin 2\theta, \text{ if } F_B > F_{D,\eta} \qquad (39)$$

If neither inequality in step 2 is satisfied, then the particle will escape by rotating about a dendrite tip away from the solidification front and drifting back into the flow. These equations, based on a two-dimensional balance, were found to represent an intermediate case between the variety of conditions that are possible when the full three-dimensional balance was calculated, as given elsewhere [12].

The primary dendrite arm spacing needed for this analysis is found from measurements conducted on cast steel, and the dendrite tip radius (r_d) is fitted from corresponding relations [34]. Calculations show that the Van der Waals interfacial force, the lubrication drag force and the surface energy gradient force are only important when the particle is very close to the solidification interface. Therefore, they can be neglected in the Lagrangian particle transport simulations. These forces are important, however, for evaluating the capture criterion to predict the fate of a particle when it touches a computational boundary representing a mushy zone front.

The results presented previously considered particles smaller than the PDAS (50-140 µm) which can easily enter in between primary dendrite arms and become entrapped with little chance of being pushed away regardless of solidification front velocity [35]. This report

focuses on larger particles (100, 250, and 400μm in diameter), which are much more difficult to capture, especially when there is a large transverse velocity.

Solution Procedure

The particle transport Eqs. (1) and (24) were integrated using a fourth order Runge-Kutta method [36]. Particle velocities and displacements were solved at every time step after the fluid velocity field was solved. The local fluid velocity in the drag and lift terms of Eq.(2) was interpolated from the nearest neighbor cells using a second order scheme [36]. Due to the low volume fraction of impurity inclusions for the continuous casting process (~0.01% for a typical steel with 30ppm oxygen), one-way coupling was employed, which neglects the modification of fluid turbulence by the particles. The removal and capture criteria were tested whenever a particle crossed a domain boundary.

Capture Criterion Model Validation

The particle capture model was tested by applying it in simulations of several different experimental systems where particle capture was measured. Firstly, the model predictions of the critical velocity of the solidification front for the transition from particle pushing to particle capture were compared with measurements of alumina particles in quiescent solidifying liquid steel [37] and zirconia particles in quiescent solidifying aluminum melt [38]. Simulations were then conducted to reproduce the results of the capture or flow of PMMA particles in solidifying water with a tangential (cross) flow across the interfacial front [39, 40]. Both system produced reasonable results, as described in detail elsewhere [12].

RESULTS

The model was applied to simulate fluid flow, particle transport, and capture during the continuous casting of a thin slab of 434 stainless steel cast at ~1.5m/min, where extensive water model and plant measurements were available [6, 41]. Although the sides of the model domain are curved according to the profile of the solidifying shell, the caster is straight-walled. The properties and conditions are given in Table 1, and match the conditions used in previous studies [6, 15, 16].

Table I. Properties and conditions of the particle simulation in the thin-slab steel caster.

Parameter/Property	Value
Mold Width (mm)	984
Mold Thickness (mm)	132
Mold Length (mm)	1200
Domain Width (mm)	
top	984
bottom	934.04
Domain Thickness (mm)	
top	132
bottom	79.48
Domain Length (mm)	2400
Nozzle Port Height × Thickness (mm × mm)	75 × 32 (inner bore)
Bottom Nozzle Port Diameter (mm)	32
SEN Submergence Depth (mm)	127
Casting Speed (mm/s)	25.4
Fluid Dynamic Viscosity (m^2/s)	7.98×10^{-7}
Fluid Density (kg/m^3)	7020
Particle Density (kg/m^3)	2700
Particle Diameter (μm)	100, 250 and 400

Predicted Flow Pattern in the Continuous-Casting Mold Region

Sample sections illustrating the flow pattern predicted by the model are given in **Fig. 5**. Close-ups of the time average flow pattern in this flared 3-port nozzle are shown near the stopper rod, and near the nozzle ports. Flow in the mold region shows a classic double-roll recirculating flow pattern. This figure also compares an instantaneous snapshot of the flow pattern (Fig. 5b) with the time average flow pattern (Fig. 5c), compiled by averaging velocity components collected over a time interval of ~70s after the flow reached "pseudo"-steady state. The observed velocity fluctuations are important to particle dispersal and capture.
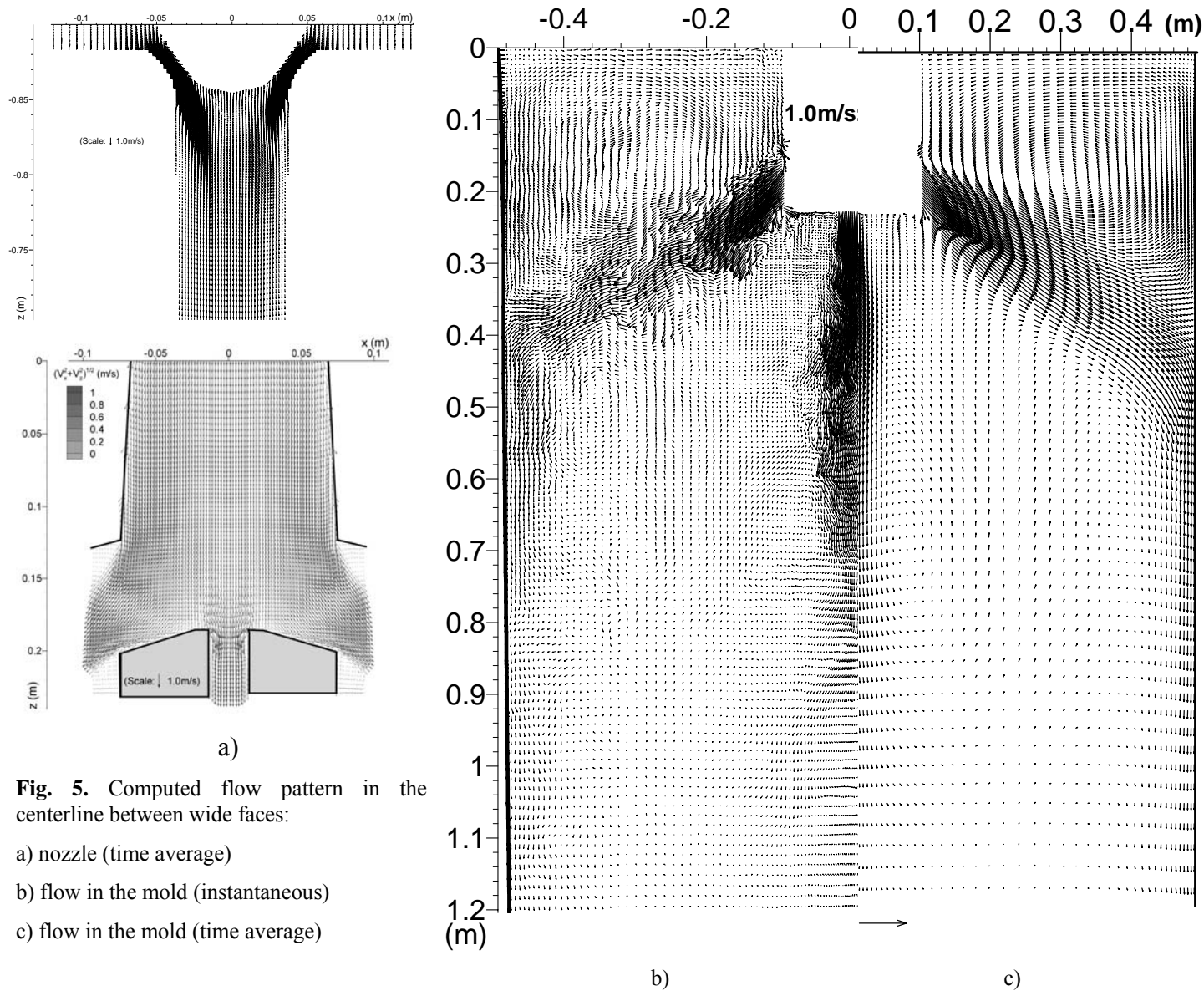
Fig. 5. Computed flow pattern in the centerline between wide faces:

a) nozzle (time average)

b) flow in the mold (instantaneous)

c) flow in the mold (time average)

Predicted Critical Cross-Flow Velocities in Continuous Steel Caster

To illustrate the behavior of the validated particle-capture criterion, the critical velocities of the flow relative to the downward moving shell for the capture of slag spheres were computed for typical conditions in a steel caster. The flow was assumed to be vertical (upwards or downwards) across a horizontally-growing solidification front, such as encountered near the narrow face in the continuous casting mold region. The results are shown in **Fig. 6** for the effect of PDAS and a complete range of particle sizes for typical solidification conditions (200μm/s solidification speed and 3.4μm tip radius).

The results illustrate how capture always occurs for particles smaller than the PDAS. Particles larger than the PDAS will be captured if the magnitude of the relative cross-flow velocity between the particle and the solidifying steel shell is smaller than a critical velocity. The magnitude of this critical velocity of the fluid decreases with increasing particle size and decreasing PDAS. Velocity magnitudes higher than the critical value prevent capture, transporting the particle away from the interface before it can get entrapped. This critical velocity depends on the flow direction. Higher critical velocity magnitudes indicate easier capture. Particles are more easily entrapped in downward flow, resulting in higher critical velocity. This is because the upward buoyancy lowers the magnitude of the particle velocity (relative to that for upward flow conditions). The wedge-shaped region of the graph indicates where the capture of large particles is possible. This region becomes narrower as particle size increases, owing to the decreasing ability of the dendrite arms to prevent the rotation of large particles. This region also becomes narrower with decreasing PDAS, again due to easier rotation of particles. The wedge tends towards the terminal velocity of the particle. When the upward terminal velocity equals the downward

flow speed (relative to the solidifying shell which is itself moving downwards at the casting speed), then the particle will be stationary relative to the dendrites, so can always be captured (based on results for quiescent flow [12]. With increasing velocity of the solidification front, particle capture becomes easier so the magnitude of the critical cross-flow velocity increases [12]. This effect is small compared with that of particle size, however. This simple, but comprehensive capture model is ready to help predict particle behavior in real casting processes over a wide range of conditions.
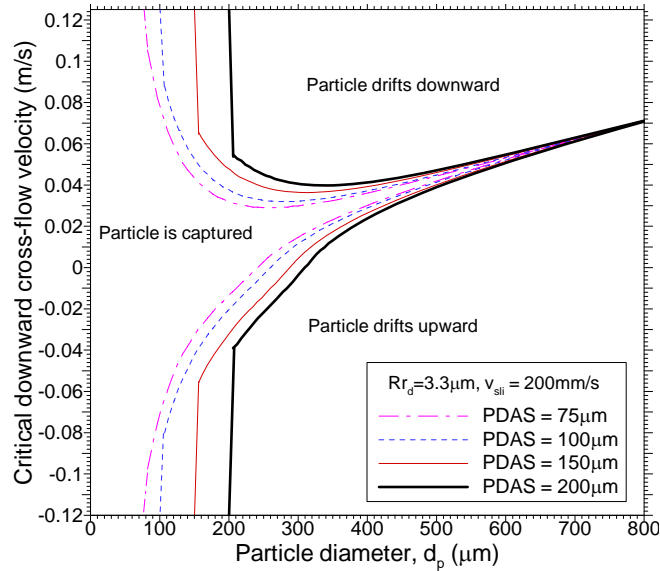

Fig. 6. Critical downward cross-flow velocities for slag droplets in molten steel.

Particle Transport, Removal and Capture in the Thin-Slab Caster

The complete LES model with particle transport and capture criterion was then applied to simulate the transport and capture of three groups of 10,000 inclusions, with 2700 kg/m3 density and three different sizes (100, 250, and 400μm) in a thin slab steel caster (Fig. 2). These inclusions could represent entrained mold slag or alumina particles that entered the mold through the nozzle over a 9s interval. The computational domain has two portions. The nozzle domain includes part of the bottom of the tundish and the entire 1.11m long trifurcated submerged entry nozzle. The strand domain includes the top 2.4m of the molten pool in the mold and strand. This 2.4m computational domain is part of the 3m straight section of the real caster. The internal liquid pool domain shape was curved to account for the shell, and had mass flowing through it to represent solidification. The shell thickness increases from 0 at the meniscus to 26mm (wide face) or 25mm (narrow face) at domain exit, according to measured profiles [15].

Elastic re-bound was assumed when a particle hit the plastic wall of the water model or the outer surface of the nozzle in steel casters. Particles touching the top surface were assumed to be safely removed by the slag layer. The particle capture criterion was tested each time a particle touched a boundary representing the solidifying shell. If the result was particle pushing, then the particle was artificially forwarded into the fluid by a distance of 5% particle radius. More information on casting conditions, material properties and computational parameters on both cases is given in Table I. Methodologies were implemented to optimize the time step size and computational cost, according to the particle response time. Both the flow simulations (1.3M cells) and the transport of 30,000 particles took about 29.2 CPUs per fluid time step (0.001s). Further details of the simulations are given elsewhere [12, 15, 16].

Particle Injection through Nozzle

After demonstrating the accuracy of this computational model of particle transport in a standard-slab water model, [15], and applying it to investigate the transport and capture of small inclusions in the actual thin slab steel caster[16, 41, 42], it was next applied to investigate the transport, removal and entrapment of large inclusions. The fluid velocities were obtained from LES [15] for conditions in Table I.

Two typical snapshots of the simulated particle distribution are shown in **Fig. 7** (3.6 and 18s after injection of the first particle from the nozzle exit plane). These snapshots are similar to those for small particles presented elsewhere [15]. While they move with the flow, the particles gradually spread apart from the local turbulent eddies. Significant asymmetrical distribution is seen in the lower region. This asymmetry is caused by the unbalanced flow between the two halves of the lower region. The larger downward flow velocities in the right half of Fig. 7 frames persisted for more than 50s before the flow became balanced for some time. Then, a similar unbalanced flow pattern occurred again after another 70s. This strong persistent asymmetrical flow deep in the lower recirculation region, was also observed in water models, such as by Gupta and Lahari [43] .

Figure 8 shows the removal histories for the 100-400μm particles. More large (400μm) particles were transported to the upper recirculation region and floated to the top surface than small ones (100μm). This is due to two factors. Firstly, the larger particles have larger terminal velocities: the terminal velocities for the 100μm, 250μm and 400μm slag spheres in liquid steel are estimated to be 3.9mm/s, 17.9mm/s and 33.5mm/s respectively, based on equating the drag and buoyancy forces. Secondly, the larger particles are more difficult to capture, as shown in Fig. 6.
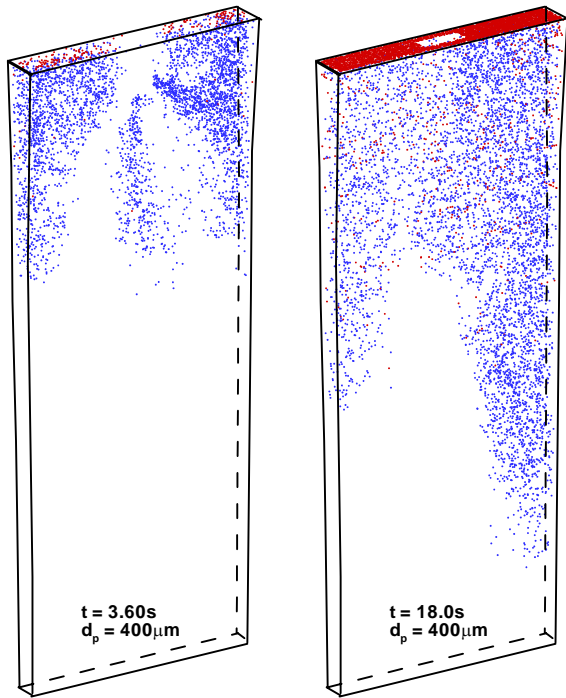

Fig. 7. Computed distribution of 400 μm particles at two different times after injection through nozzle ports
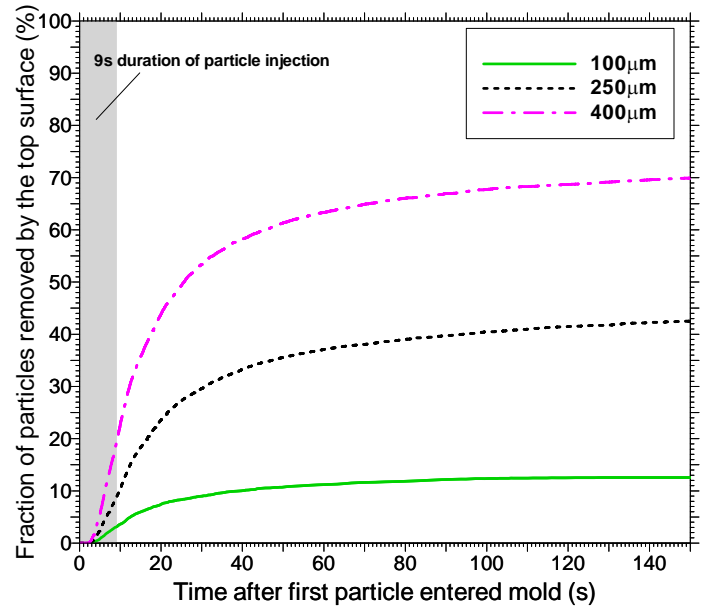

Fig.8. Removal and entrapment histories of large particles (≥100μm) which entered the mold region from nozzle ports

Most (~90%) of the particle removal occurred in the first ~50s after the first particle entered the domain. Most (90%) of the captured particles traveled with the flow for less than ~70s. The final removal fractions were 12.6%, 42.5% and 69.9% for the 100, 250 and 400μm particles respectively. These results are consistent with plant observations that particles with sizes ranging from 50μm to 200μm are the main cause of inclusion defects in steel slabs.

The results shown here suggest that very large particles can be effectively removed from the mold region. This is known to be the case for straight-walled casters, and is the reason that many companies have invested in changing their top sections from curved to vertical. Alternatively, the less-buoyant smaller particles always experience small removal fractions. These cause less quality problems owing to their smaller size. Intermediate-sized particles of 100μm - 250μm are large enough to cause severe quality problems, yet are predicted to have high entrapment fractions, even in a vertical caster. Thus, it is important that they are removed from the steel prior to entering the mold. This conclusion may differ if gas bubbles are present, so the effects of gas injection are investigated in a later section.

Slag Entrainment from Top Surface

During the actual continuous casting process, fingers of the liquid slag layer may be emulsified into the liquid steel from the top surface mold slag layer and broken into spheres by the flow. This is an important alternative source of mold slag inclusions, in addition to those entering the nozzle from upstream. To model this, a computation was conducted where three groups of 4,000 particles with sizes of 100μm, 250μm and 400 μm entered the domain near the center of the top surface, where such emulsification most likely occurs. The particles were injected computationally over 1.8s into two symmetrical 20mm×6mm×7mm(x×y×z) volumes located just below the top surface. The height of the two volumes was chosen based on the measured steel-slag interface profile [15].

Figure 9 presents two typical snapshots of the distribution of the 100μm particles, 5.6s and 18s after entrainment. Again, blue dots denote moving particles and red represents the removed or captured ones. It is seen that immediately after the injection, some of the particles floated to the top surface and were consequently removed. The other particles followed the flow in the upper recirculation

region, joined the oblique jet, and then behaved as if they were injected from the nozzle ports. **Figure 10** shows the evolution of the removal of these inclusions back into the top surface slag layer. More than 95% of the large 400μm particles were safely removed in the first 2s after being entrained into the flow from the top surface slag layer. The final removal fractions exceeded 92% for particles 250μm or larger. However, the removal fraction dropped to 44.6% for the less buoyant 100μm particles. This is because a significant fraction of these inclusions became entrained into the fast-moving jets from the nozzle ports, and thereafter behaved the same as particles entering the mold through the nozzle. This finding demonstrates that it is very important to control fluid flow in the mold in order to avoid the entrainment of additional mold slag inclusions. In fact, the design of the flow pattern to avoid of re-entrainment of surface slag is likely to be more beneficial than a design which attempts to enhance the removal of inclusions which enter the mold through the nozzle.
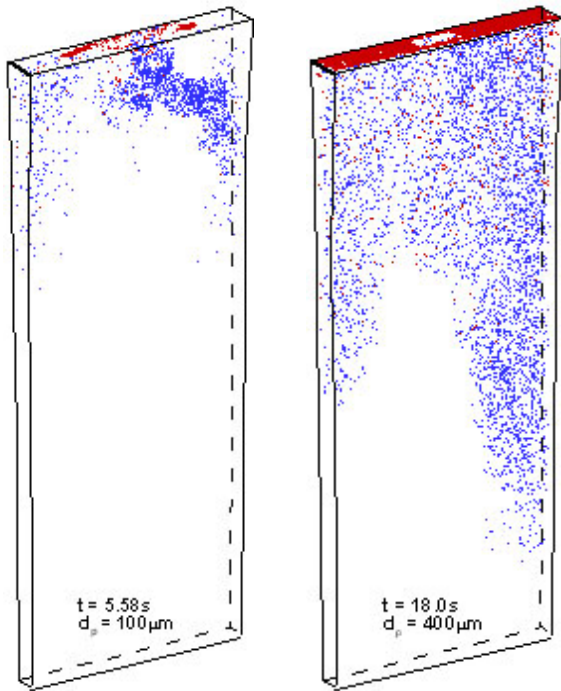

Fig. 9. Computed snapshots at two different times of distribution of 400 μm slag particles in the steel caster entrained at the top surface.
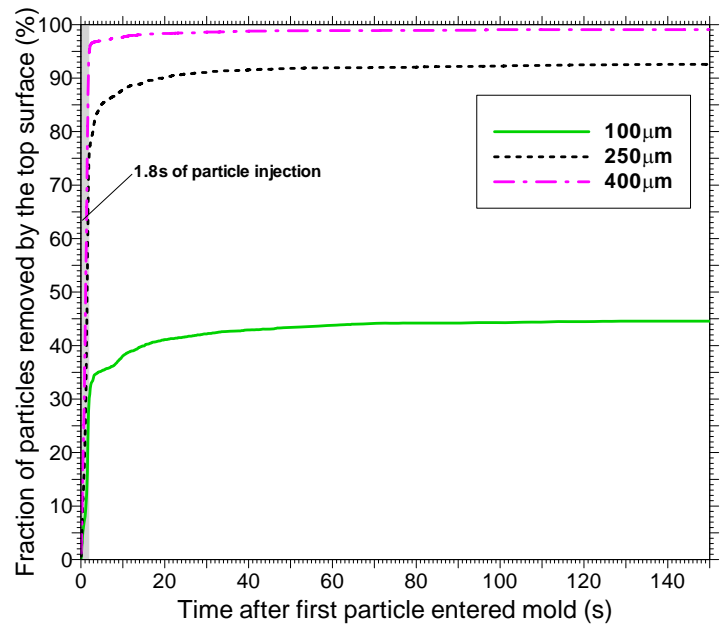
Fig. 10. Removal and entrapment histories of large particles (≥100μm) which entered the mold region from entrainment at the top surface center

CONCLUSIONS

Lagrangian computations of particle transport during continuous casting of steel slabs were performed in this study, based on time-dependent fluid velocity fields obtained from Large Eddy Simulations of the three-dimensional fluid flow. For the casting conditions simulated here, the results reveal that:

- Particle entrapment by a solidification front depends on many factors including the particle size and density, transverse fluid velocity, sulfur concentration gradient, solidification front velocity, and primary dendrite arm spacing. A new capture criterion based on a balance of the important forces acting on a particle near a solidification front has been developed, validated with test problems and applied to simulate particle capture in a steel continuous caster.

- Increasing the number of particles improves the accuracy of removal predictions, especially for later times (e.g. 10-100s). At least 2500 particles are required to obtain accuracy within ±3%. Particle removal at short times (e.g. ≤10s) is governed by chaotic fluctuations of the flow, which generate variations of ±5%.

- After a 9s sudden burst of particles enters the steel caster, about 4 minutes are needed for all of them to be captured or removed. The captured particles concentrate mainly within a 2-m long section of slab.

- Most of the inclusions trapped in the steel slab are concentrated within 10-20mm beneath the slab surface, especially at the corner, and towards the narrow faces.

- The safe removal of inclusion particles to the top surface decreases greatly with decreasing particle size. Although the removal fraction of 400 μm particles is 70%, only ~12% of 100 μm particles are removed. Only 8% of small particles (10μm and 40μm) are removed.

- The removal of slag particles entrained from the top surface depends greatly on the particle size. Most (>92%) of the 250μm - 400μm droplets simply return to the slag layer. However, more than half of the 100μm particles are eventually entrapped into the solidifying steel shell, leading to sliver defects in the rolled product.

- Based on these results, the design of nozzle geometry and casting conditions should focus on optimizing the flow pattern at the top surface of the mold to avoid slag entrainment, excessive level fluctuations, meniscus freezing, and related problems. Inclusions should be removed during upstream processing.

ACKNOWLEDGMENTS

REFERENCES

1. B.G. Thomas, "Modeling of the Continuous Casting of Steel: Past, Present, and Future, Dr. J. Keith Brimacombe Lecture," Metal. & Material Trans., Vol. 33B (Dec.), 2002, 795-812.
2. W.H. Emling, T.A. Waugaman, S.L. Feldbauer, A.W. Cramb, "Subsurface Mold Slag Entrainment in Ultra-Low Carbon Steels," in Steelmaking Conf. Proc., Vol. 77, ISS, Warrendale, PA, (Chicago, IL), 1994, 371-379.
3. R.C. Sussman, M. Burns, X. Huang, B.G. Thomas, "Inclusion Particle Behavior in a Continuous Slab Casting Mold," in 10th Process Technology Conference Proc., Vol. 10, Iron and Steel Society, Warrendale, PA, (Toronto, Canada, April 5-8, 1992), 1992, 291-304.
4. B.G. Thomas, A. Denissov and H. Bai, "Behavior of Argon Bubbles during Continuous Casting of Steel," in Steelmaking Conf. Proc., Vol. 80, ISS, Warrendale, PA., (Chicago, IL), 1997, 375-384.
5. J. Herbertson, Q.L. He, P.J. Flint, R.B. Mahapatra, "Modelling of Metal Delivery to Continuous Casting Moulds," in Steelmaking Conf. Proc., Vol. 74, ISS, Warrendale, PA, (Washington, D.C.), 1991, 171-185.
6. Q. Yuan, B.G. Thomas and S.P. Vanka, "Turbulent Flow and Particle Motion in Continuous Slab-Casting Molds," in ISSTech 2003 Process Technology Proceedings, Vol. 86, ISS, Warrendale, PA, (Indianapolis, IN, Apr 27-30, 2003), 2003, 913-927.
7. F.H. Harlow and J.E. Welch, "Numerical calculation of time-dependent viscous incompressible flow of fluids with free surface," Physics of Fluids, Vol. 8, 2182-2189.
8. J. Crank and P. Nicolson, "A Practical Method for Numerical Evaluation of Solutions of Partial Differential Equations of the Heat-Conduction Type," Proceedings of Cambridge Philosophic Society, Vol. 43, 1947, 50-67.
9. L.F. Sampine and M.K. Gordon, Computer Solution of Ordinary Differential Equations: The Initial Value Problem, W.H. Freeman, San Francisco, 1975.
10. "User's Manual: Hypre - High Performance Preconditioners, Center for Applied Scientific Computing," Report, Lawrence Livermore National Laboratory, 2001.
11. K. Horiuti, "Large Eddy Simulation of Turbulent Channel Flow by One-Equation Modeling," Journal of the Physical Society of Japan, Vol. 54 (8), 1985, 2855-2865.
12. Q. Yuan, "Transient Study of Turbulent Flow and Particle Transport During Continuous Casting of Steel Slabs," PhD Thesis, University of Illinois at Urbana-Champaign, IL, 2004.
13. Q. Yuan, B. Zhao, S.P. Vanka, B.G. Thomas, "Study of Computational Issues in Simulation of Transient Flow in Continuous Casting," Steel Research International, Vol. 76 (1), 2005, 33-43.
14. Q. Yuan, B. Zhao, S.P. Vanka, B.G. Thomas, "Study of Computational Issues in Simulation of Transient Flow in Continuous Casting," Materials Science & Technology 2004, (New Orleans, LA), TMS, Warrendale, PA, Vol. II, 2004, 333-343.
15. Q. Yuan, B.G. Thomas and S.P. Vanka, "Study of Transient Flow and Particle Transport during Continuous Casting of Steel Slabs, Part 1. Fluid Flow," Metal. & Material Trans. B., Vol. 35B (4), 2004, 685-702.
16. Q. Yuan, B.G. Thomas and S.P. Vanka, "Study of Transient Flow and Particle Transport during Continuous Casting of Steel Slabs, Part 2. Particle Transport.," Metal. & Material Trans. B., Vol. 35B (4), 2004, 703-714.
17. C. Crowe, M. Sommerfild and Y. Tsinji, Multiphase Flows with Droplets and Particles, CRC Press, 1998, 71.
18. P.G. Saffman, "Corrigendum to "The Lift on a Small Sphere in a Slow Shear Flow"," J. Fluid Mech., Vol. 31, 1968, 624.
19. J.B. McLaughlin, "Inertial Migration of a small sphere in linear shear flow," J. Fluid Mech., Vol. 224, 1991, 261-275.
20. J.B. McLaughlin, "The Lift Force on a Small Sphere in Wall-Bounded Linear Shear Flows," J. Fluid Mech., Vol. 246, 1993, 249-265.

21. J.B. McLaughlin, "Inertial Migration of a Small Sphere in Linear Shear Flow," <u>Journal of Fluid Mechanics,</u> Vol. 224 (262-274), 1991,

22. R. Mei, "Brief Communication: An Approximate Expression for the Shear Lift Force on a Spherical Particle at Finite Reynolds Number," <u>International Journal of Multiphase Flow,</u> Vol. 18 (1), 1992, 145-147.

23. Q. Wang, K.D. Squires, M. CHen, J.B. McLaughlin, "On the Role of the Lift Force in Turbulence Simulations of Particle Deposition," <u>Int. J. Multiphase Flow,</u> Vol. 23 (4), 1997, 749-763.

24. I.E. Barton, "Computation of Particle Tracks over a Backward-Facing Step," <u>Journal of Aerosol Science,</u> Vol. 26 (6), 1995, 887-901.

25. F. Odar and W.S. Hamilton, "Forces on a Sphere Accelerating in a Viscous Fluid," <u>Journal of Fluid Mechanics,</u> Vol. 18, 1964, 302-314.

26. F. Odar, "Verification of the Proposed Equation for Calculation of the Forces on a Sphere Accelerating in a Viscous Flow," <u>Journal of Fluid Mechanics,</u> Vol. 25, 1966, 591-592.

27. M.W. Reeks and S. Mckee, "The Dispersive Effect of Basset History Forces on Particle Motion in a Turbulent Flow," <u>Physics of Fluids,</u> Vol. 27, 1984, 1573-1582.

28. D. Shangguan, S. Ahuja and D.M. Stefanescu, "An Analytical Model for the Interaction between an Insoluble Particle and an Advancing Solid/Liquid Interface," <u>Metallurgical Transactions A,</u> Vol. 23A (2), 1992, 669-680.

29. G.F. Bolling and J.A. Cisse, "A Theory for The Interaction of Particles with a Solidification Front," <u>Journal of Crystal Growth,</u> Vol. 10, 1971, 55-66.

30. J. Potschke and V. Rogge, "On The Behavior of Foreign Particle at An Advancing Solid-Liquid Interface," <u>Journal of Crystal Growth,</u> Vol. 94, 1989, 726-738.

31. K. Mukai and W. Lin, "Behavior of Non-metallic Inclusions and Bubbles in Front of Solidifying Interface of Liquid Iron," <u>Tetsu-to-Hagane,</u> Vol. 80 (7), 1994, 533-538.

32. G. Wilde and J.H. Perepezko, "Experimental Study of Particle Incorporation During Dendritic Solidification," <u>Materials Science & Engineering A,</u> Vol. 283, 2000, 25-37.

33. J-H.Jeong, N. Goldenfeld and J.A. Dantzig, "Phase Field Model for Three-Dimensional Dendritic Growth with Fluid Flow," <u>Physical Review E,</u> Vol. 64, 2001, 1-14.

34. W. Kurz and D.F. Fisher, <u>Fundamentals of Solidification</u>, Trans Tech Publications SA, Aedermannsdorf, Switzerland, 1984, 242.

35. Q. Yuan, "Modeling of Particle Engulfment / Pushing at Solidification Front during Continuous Casting of Steel," Report, University of Illinois at Urbana-Champaign, 2002.

36. W.H. Press, B.P. Flannery, S.A. Teukolsky, W.T. Vetterling, <u>Numerical Recipes</u>, Cambridge University Press, New York, NY, 1988, 289-293.

37. H. Shibata, H. Yin, S. Yoshinaga, T. Emi, M. Suzuki, "In-Situ Observation of Engulfment and Pushing of Nonmetallic Inclusions in Steel Melt by Advancing Melt/Solid Interface," <u>ISIJ International,</u> Vol. 38 (2), 1998, 149-156.

38. D.M. Stefanescu, F.R. Juretzko, B.K. Dhindaw, A. Catalina, S. Sen, "Particle Engulfment and Pushing by Solidifying Interfaces: Part II. Microgravity Experiments and Theoretical Analysis," <u>Metallurgical and Materials Transactions A,</u> Vol. 29A, 1998, 1697-1706.

39. Q. Han and J.D. Hunt, "Particle Pushing: Critical Flow Rate Required to Put Particles into Motion," <u>J. Crystal Growth,</u> Vol. 152, 1995, 221-227.

40. Q. Han, "The Mechanisms for Particle Pushing," PhD Thesis, University of Oxford, Oxford, UK, 1994.

41. B.G. Thomas, R. O'Malley, T. Shi, Y. Meng, D. Creech, D. Stone, "Validation of Fluid Flow and Solidification Simulation of a Continuous Thin Slab Caster," in <u>Modeling of Casting, Welding, and Advanced Solidification Processes</u>, Vol. IX, Shaker Verlag GmbH, Aachen, Germany, (Aachen, Germany, August 20-25, 2000), 2000, 769-776.

42. B.G. Thomas, R.J. O'Malley and D.T. Stone, "Measurement of temperature, solidification, and microstructure in a continuous cast thin slab," Modeling of Casting, Welding, and Advanced Solidification Processes, (San Diego, CA), TMS, Warrendale, PA, Vol. VIII, 1998, 1185-1199.

43. D. Gupta and A.K. Lahiri, "A Water Model Study of the Flow Asymmetry Inside a Continuous Slab Casting Mold," <u>Metall. Mater. Trans. B,</u> Vol. 27B (5), 1996, 757-764.